Multiwavelength Observations of SDSS J105621.45+313822.1, a Broad-line, Low-metallicity AGN

Jenna M. Cann[1,6] , Shobita Satyapal[1] , Thomas Bohn[2], Remington O. Sexton[2] , Ryan W. Pfeifle[1] ,
Christina Manzano-King[2] , Gabriela Canalizo[2], Barry Rothberg[1,3] , Mario Gliozzi[1] , Nathan J. Secrest[4] , and
Laura Blecha[5]

[1] George Mason University, Department of Physics and Astronomy, MS3F3, 4400 University Drive, Fairfax, VA 22030, USA; jcann@masonlive.gmu.edu
[2] Department of Physics and Astronomy, University of California, Riverside, 900 University Avenue, Riverside, CA 92521, USA
[3] LBT Observatory, University of Arizona, 933 N. Cherry Avenue, Tuscon, AZ 85721, USA
[4] U.S. Naval Observatory, 3450 Massachusetts Avenue NW, Washington, DC 20392, USA
[5] University of Florida, Department of Physics, P.O. Box 118440, Gainesville, FL 32611-8440, USA

Abstract

In contrast to massive galaxies with solar or super-solar gas phase metallicities, very few active galactic nuclei (AGNs) are found in low-metallicity dwarf galaxies. Such a population could provide insight into the origins of supermassive black holes. Here we report near-IR spectroscopic and X-ray observations of SDSS J105621.45 +313822.1, a low-mass, low-metallicity galaxy with optical narrow line ratios consistent with star-forming galaxies but a broad Hα line and mid-infrared colors consistent with an AGN. We detect the [Si VI] 1.96 μm coronal line and a broad Paα line with an FWHM of 850 ± 25 km s^{-1}. Together with the optical broad lines and coronal lines seen in the Sloan Digital Sky Survey (SDSS) spectrum, we confirm the presence of a highly accreting black hole with mass $(2.2 \pm 1.3) \times 10^6 M_{\odot}$, with a bolometric luminosity of $\approx 10^{44}$ erg s^{-1} based on the coronal line luminosity, implying a highly accreting AGN. Chandra observations reveal a weak nuclear point source with $L_{X,2-10keV} = (2.3 \pm 1.2) \times 10^{41}$ erg s^{-1}, $\sim$2 orders of magnitude lower than that predicted by the mid-infrared luminosity, suggesting that the AGN is highly obscured despite showing broad lines in the optical spectrum. The low X-ray luminosity and optical narrow line ratios of J1056+3138 highlight the limitations of commonly employed diagnostics in the hunt for AGNs in the low-metallicity, low-mass regime.

Unified Astronomy Thesaurus concepts: Supermassive black holes (1663); AGN host galaxies (2017)

1. Introduction

The vast majority of active galactic nuclei (AGNs) are found in massive bulge dominated galaxies with gas phase metallicities that are typically super solar (e.g., Storchi-Bergmann et al. 1998; Hamann et al. 2002). Since the gas phase metallicity is strongly correlated with the galaxy's stellar mass, low-metallicity AGNs are likely to reside in low-mass galaxies. The hunt for AGNs in dwarf galaxies has been an active field of research in recent years, since the black hole occupation fraction and mass distribution in the low-mass regime place important constraints on models of supermassive black hole (SMBH) seed formation (e.g., Volonteri & Natarajan 2009; Volonteri & Begelman 2010; van Wassenhove et al. 2010; Greene 2012). However, searches for AGNs in low-mass galaxies have yielded only a small fraction of AGNs, all with solar or only slightly sub-solar metallicities. This is a severe limitation, since the premise behind the use of dwarf galaxies to probe seed black holes rests on the assumption that they have had a quiescent cosmic history, free of external factors such as merging or tidal stirring, both of which would drive gas to the center, fueling star formation, enriching the gas, growing a bulge, and potentially fueling the SMBH. For example, in an extensive search of type 2 AGNs using the Sloan Digital Sky Survey (SDSS) Groves et al. (2006) and Barth et al. (2008) found only a small fraction of AGNs residing in low-mass hosts, all with either solar or only slightly sub-solar metallicities. Similarly, in the recent optical survey of dwarf galaxies by Reines et al. (2013), nearly all of the dwarf galaxies with narrow emission line ratios

consistent with AGNs have at least solar metallicities, consistent with the high metallicity range found for the low-mass broad-line AGNs identified by Greene & Ho (2007). While extremely rare, there have been a few low-metallicity AGNs reported in the literature. Izotov et al. (2007, 2010) and Izotov & Thuan (2008) found evidence for extremely luminous broad-line emission consistent with AGNs in a handful of low-metallicity dwarf galaxies, most with optical narrow line ratios typical of H II regions, and Schramm et al. (2013) found X-ray evidence for an AGN in several low-mass galaxies, one of which is metal deficient, suggesting that low-metallicity AGNs do exist. Of these few low-metallicity AGNs, extensive multiwavelength observations are thus far lacking in the literature.

Here we present a multiwavelength study of a low-metallicity, broad-line AGN, SDSS J105621.45+313822.1 (hereafter J1056+3138), a galaxy that is identified as a QSO broad-line object by SDSS DR12, and in past catalogs has been classified as a broad-line QSO (D'Abrusco et al. 2009; Richards et al. 2009, 2015; Souchay et al. 2012, 2015) or broad-line AGN (Toba et al. 2014; Rakshit et al. 2017). Based on the Max Planck Institut für Astrophysik/Johns Hopkins University (MPA/JHU) catalog, the galaxy has a redshift of $z = 0.161$ and a stellar mass of $10^{9.89} M_{\odot}$, roughly 2.5× the mass of the Large Magellanic Cloud. In Figure 1, we plot the location of J1056+3138 on the Baldwin–Phillips–Terlevich (BPT) diagram (Baldwin et al. 1981). As can be seen, it has one of the lowest [N II]/Hα emission line ratios, a robust indicator of gas phase metallicity regardless of ionizing radiation field and ionization parameter (Groves et al. 2006), compared to the entire sample of Swift/BAT AGNs from the 70 month catalog

---
[6] National Science Foundation, Graduate Research Fellow.
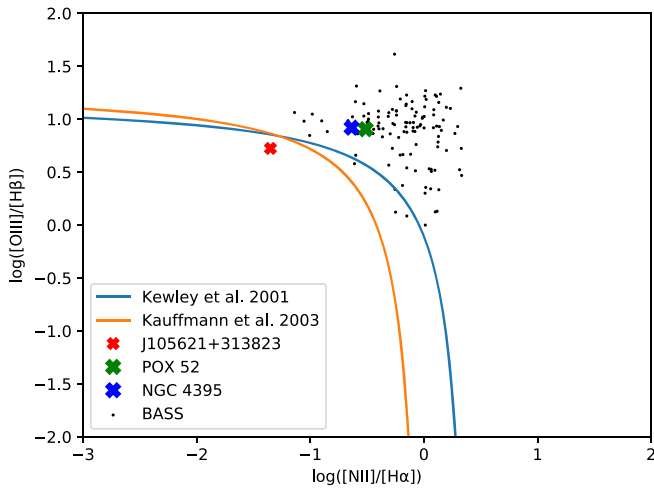
Figure 1. BPT diagram comparing J1056+31 (red "x") with the BASS sample (Koss et al. 2017), with the AGN (Kewley et al. 2001) and composite (Kauffmann et al. 2003) demarcation regions in blue and orange, respectively. Also plotted are NGC 4395 (blue "x"; Filippenko & Ho 2003) and Pox 52 (green "x"; Barth et al. 2004). Note that J1056+31 is the only target that meets our metallicity selection criteria and displays star-forming ratios.

(Baumgartner et al. 2013), which comprise the most complete sample of hard X-ray (14–195 keV) selected AGNs in the local universe. Note that the well known dwarf galaxies with AGNs, NGC 4395 (Filippenko & Ho 2003) and POX 52 (Barth et al. 2004), both have at least 2–10× higher gas metallicities than our target as suggested by their [N II]/Hα ratios shown in Figure 1.

In addition to the identification of broad lines, J1056+3138 displays mid-infrared colors suggestive of an AGN using the all-sky Wide-field Infrared Sky Explorer (WISE) and the 3-band demarcation from Jarrett et al. (2011). In general, low-metallicity galaxies tend to be bluer, with relatively few displaying mid-infrared colors [3.4 μm]–[4.6 μm] (hereafter W1 − W2) > 1.0 (Griffith et al. 2011; Izotov et al. 2011). Those that do show red WISE colors tend to reside to the left of region that typically signifies dominant AGNs when plotted in W1 − W2 versus [4.6 μm]–[12 μm] (hereafter W2 − W3) space (Jarrett et al. 2011). As can be seen in Figure 2, only ≈0.7% of galaxies with similar metallicity to J1056+3138 display mid-infrared colors characteristic of an AGN, further emphasizing the unique nature of this object.

Broad-line AGNs with optical narrow line diagnostics consistent with star-forming galaxies such as J1056+3138 constitute an extremely rare population. There are only ≈5% of broad-line AGNs falling in the star-forming region of the BPT diagram according to a recent study by Stern & Laor (2013). Using the full MPA/JHU catalog[7] of derived galaxy properties for the SDSS data release 8 (DR8), approximately 4% of broad-line galaxies have comparable or lower [N II]/Hα emission line ratios indicating low-gas-phase metallicities. Only 1.5% of all broad-line AGNs have log ([N II]/Hα) ratios less than −1.3, the value for J1056+3138.

This paper is organized as follows. In Section 2, we describe our near-IR and X-ray observations and data analysis, followed by a description of our results in Section 3. In Section 4, we discuss our results, and summarize our findings in Section 5.
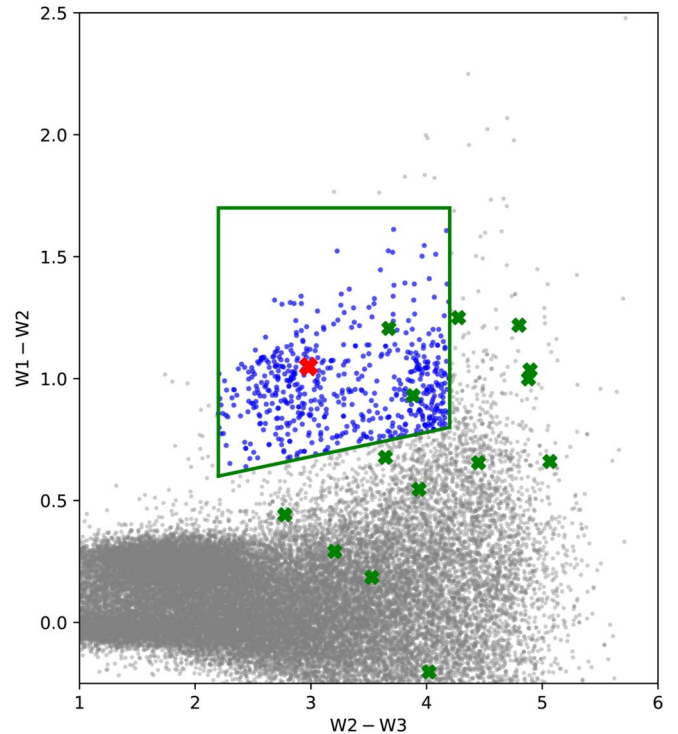
Figure 2. Mid-infrared color–color diagram showing the placement of low-metallicity galaxies with comparable log [N II]/Hα to J1056+3138, as defined by [N II]/Hα ⩽ − 1.3 using emission line fluxes from the MPA catalog. The box corresponds to the Jarrett et al. (2011) demarcation region. Gray points correspond to galaxies that would not be identified as potential AGNs using the strict Jarrett et al. (2011) color cut, and blue points denote galaxies that would be characterized as potential AGNs. The location of J1056+3138 is marked with a red "X" and locations of other published low-metallicity galaxies are marked with green "X's" (Thuan & Izotov 2005; Izotov et al. 2007, 2012; Izotov & Thuan 2008).

We adopt a standard ΛCDM cosmology with $H_0 = 70$ km s^{-1} Mpc^{-1}, $\Omega_M = 0.3$, and $\Omega_\Lambda = 0.7$.

2. Methodology

2.1. Near-infrared Observations and Data Reduction

We obtained near-IR observations of J1056+3138 using the Near-Infrared Spectrograph (NIRSPEC; McLean et al. 1998) on the Keck II telescope on 2018 March 5, with a total exposure time of 32 minutes. These observations were carried out using the low-resolution mode with a slit width of 0″.76 and a slit length of 42″ to provide a resolution of $R \approx 1400$. We used the filter NIRSPEC-7 for a wavelength coverage of 1.839–2.630 μm. Observations were done using an ABBA pattern, nodding along the slit. This target was observed under clear weather conditions, with ∼0″.5 seeing. A telluric standard (A0V) was observed immediately after at similar air mass.

The data reduction was carried out using a modified version of LONGSLIT_REDUCE (Becker et al. 2009) for Keck NIRSPEC, and REDSPEC.[8] These packages followed the standard steps for IR spectral data reduction, including flat-fielding, sky subtraction, wavelength calibration, spectral extraction, and telluric correction. Flux calibration was done in Python by estimating the flux of the telluric A0V star through its K-band

---
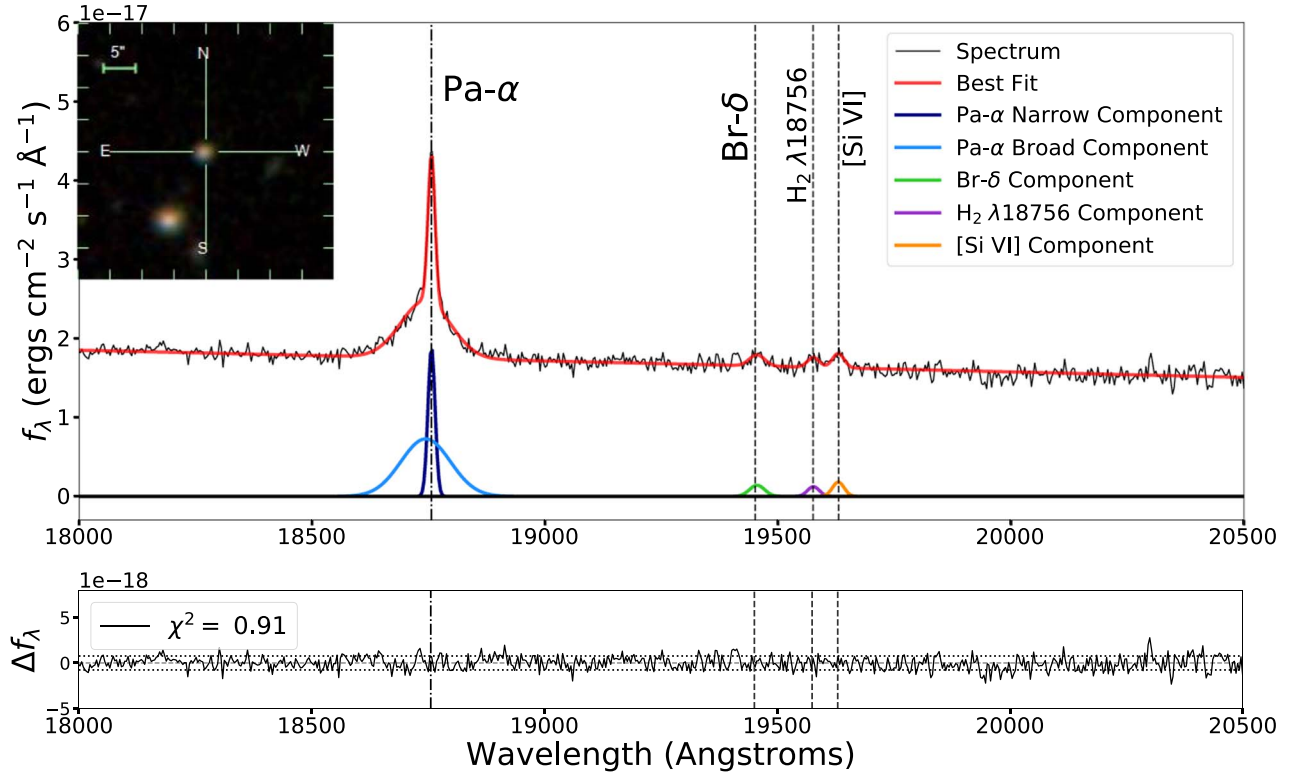
Figure 3. *K*-band spectra from Keck NIRSPEC of J1056+3138. Note that this galaxy displays a prominent broad Paα line and the [Si VI] coronal line, as well as Brδ and H$_2$ lines. An SDSS *gri* color composite image is also displayed, showing its compact morphology.

magnitude and scaling the spectrum by this flux. A small corrective factor ($<5\%$) was included due to the wavelength difference between the center of *K*-band and that of the wavelength coverage used. Line fluxes and uncertainties were determined from best-fit Gaussian models to the emission lines using a custom Bayesian maximum-likelihood code implemented in Python using the affine-invariant Markov Chain Monte Carlo ensemble sampler *emcee* (Foreman-Mackey et al. 2013).

2.2. Optical Observations and Analysis

This object was observed twice by SDSS, once on 2004 May 12 with the SDSS spectrograph and once on 2013 March 18 with the Baryon Oscillation Spectroscopic Survey spectrograph (Dawson et al. 2013). Aside from the emergence of a [Fe VII] $\lambda5722$ emission line in the 2013 that was not visible in 2004, these two spectra are nearly equivalent, with consistent broad and narrow line fluxes within photometric uncertainties, so the remainder of the paper will analyze the 2013 spectrum as it has the higher signal-to-noise ratio. We analyzed this spectrum in order to compare broad-line fluxes and widths to our near-IR observations. Optical spectral decomposition was performed on the SDSS spectrum using *emcee* (Foreman-Mackey et al. 2013) as done by Sexton et al. (2019). For the Hβ/[O III] region, we fit the region from restframe 4400–5800 Å, which includes the bMg I region used to estimate stellar velocity dispersion. All emission lines are modeled using Gaussians, with narrow line FWHM and velocity offsets tied during the fitting process. For the Hα/[N II] region, we fit the region from restframe 6200–7000 Å. The lack of prominent stellar absorption features in this region prevents us from using stellar template fitting, and

thus the continuum is fit using only the power-law component, with amplitude and power-law index as free parameters. As with the near-IR data, line fluxes and uncertainties were determined using best-fit Gaussian models.

2.3. X-Ray Observations and Data Reduction

Chandra observations of this target were taken on 2019 October 20 in Cycle 19. Data was taken with the ACIS-S instrument, with an exposure time of 16 ks, and pointed with the target centered at the aimpoint of the S3 chip. The data was reduced and analyzed using the Chandra Interactive Analysis of Observations (CIAO) data package v4.11 and the Chandra Calibration Database v4.8.2 (CALDB). After reprocessing and filtering the event file into full (0.3–8 keV), soft (0.3–2 keV), and hard (2–8 keV) energy bands, we used the DMEXTRACT module to extract the source counts from a $1\farcs5$ radius aperture centered on the source position. Background counts were extracted from a $25''$ radius aperture in the vicinity of the source and in an area free of other sources. Due to the low count nature of this source, we use binomial statistics, using the Gehrels (1986) approximation to account for the error in the source counts, where the upper bound is given by $1 + \sqrt{x + 0.75}$, the lower bound by $\sqrt{x - 0.25}$, and *x* is the number of counts detected. All X-ray fluxes and luminosities quoted hereafter are derived from background-subtracted counts.

3. Results

3.1. Near-infrared and Optical Spectra of J1056+31

The near-IR *K*-band spectrum of J1056+31 can be found in Figure 3. Most notably, this target contains a 3.3σ [Si VI] detection, with a flux of $(5.69 \pm 1.75) \times 10^{-17}$ erg cm^{-2} s^{-1}
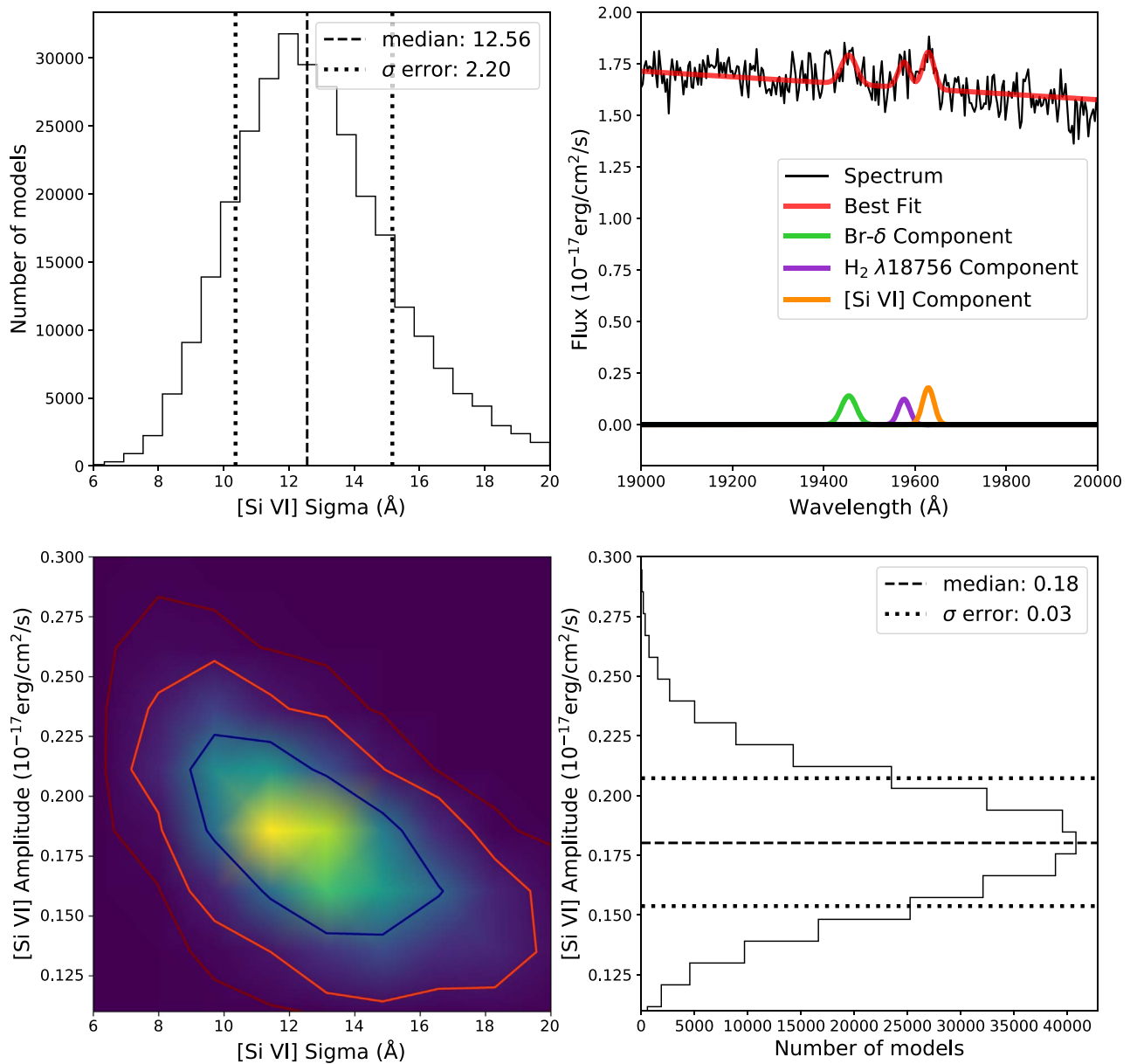
Figure 4. Upper Right: the detected [Si VI] emission line, as well as nearby Brδ and H₂ lines. Lower Left: a heat map showing the output of the *emcee* fits for the amplitude and width of the Gaussian for the [Si VI] detection in J1056+3138. The contour levels show the σ intervals up to 3σ, and the histograms (upper left and lower right) show the distribution of potential fits for the width (upper left) and amplitude (lower right) of the Gaussian. As can be seen, the solution converged very well, proving a robust detection.

(Figure 4). As Si VI has an ionization potential of 167 eV, even the hottest, most massive stars do not produce enough high-energy ionizing radiation required to produce this ion (S. Satyapal et al. 2020, in preparation).

The SDSS optical spectrum is shown in in Figure 5. Coronal lines were observed in both the SDSS and Keck observations. The SDSS observations showed [Fe VII]λ5722 and [Fe VII]λ6085 emission lines, and [Ne V]λ3425 and [Ne V]λ3345 lines. These are the most ubiquitous optical coronal lines, which have been widely seen in AGNs (e.g., Appenzeller & Wagner 1991; Vergani et al. 2018; Yan et al. 2019). Note that the ionization potentials of Fe VII and Ne V are 99 eV and 97 eV, respectively; which is significantly less than the ionization potential of Si VI. Fluxes for these lines can be found in Table 1 for the [Si VI] and Table 2 for the optical lines. Note that the luminosity of the [Si VI] line is 3.18×10^{39} erg s^{-1}, well within the range of

luminosities of the well-studied AGN from Müller-Sánchez et al. (2018) and Lamperti et al. (2017), which range from 5.9×10^{36} to 3.9×10^{41} erg s^{-1}. The [Fe VII] and [Ne V] lines in J1056 +3138 have luminosities of $\approx 10^{40}$ erg s^{-1}, comparable to those observed in other AGN samples, with luminosities ranging from 10^{39} to 10^{42} erg s^{-1} (Malkan 1986; Morris & Ward 1988; Storchi-Bergmann et al. 1995).

As can be seen in Figure 3, the spectra also contains a broad Paα line with a flux of $(35.90 \pm 1.73) \times 10^{-17}$ erg cm^{-2} s^{-1} and a width of 850 ± 25 km s^{-1}. A Brδ and H₂ line were also detected. Fluxes for all infrared lines can be found in Table 1. While its optical narrow emission lines placed the object in the "star-forming" region of the BPT diagram (see Figure 1), J1056 +3138 showed a broad Hα line, as well as [Fe VII]λ5722,6085 and [Ne V]λ3425,3345 coronal lines, as can be seen in Figure 5. While broad lines and coronal lines can be indicative
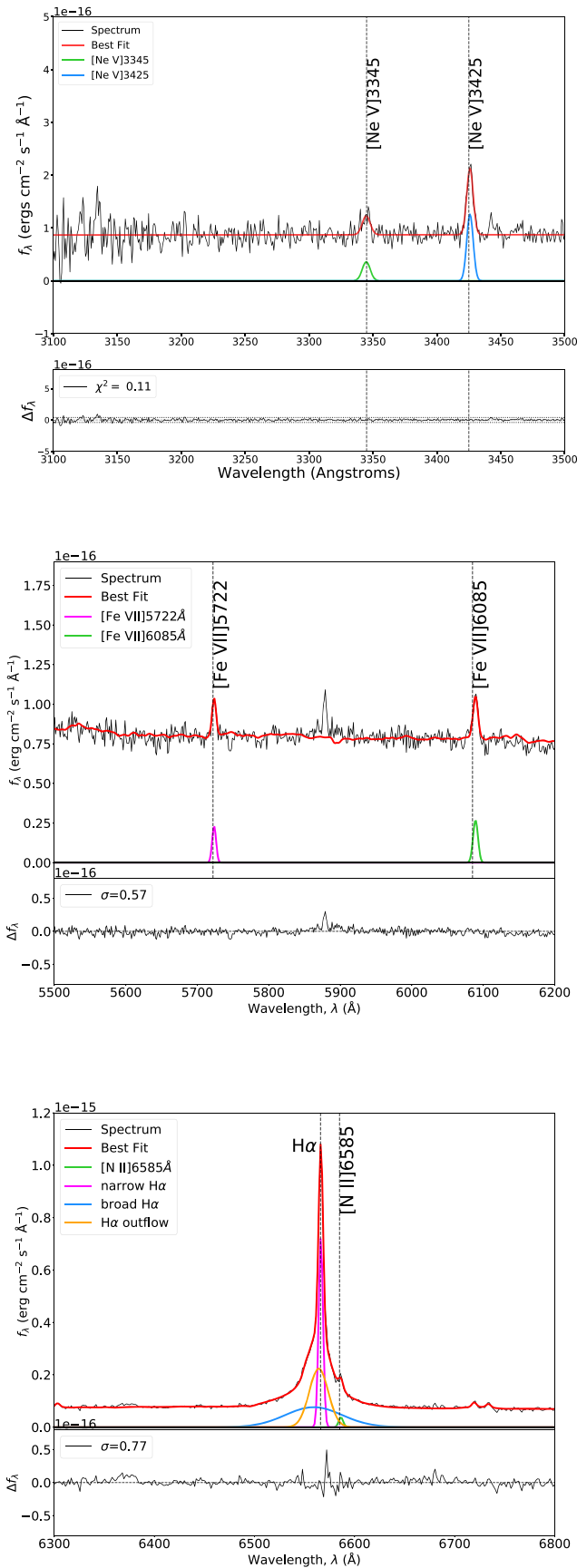
Figure 5. Optical spectra from SDSS of J1056+3138. The top panel displays the fits for the [Ne V]λλ3345,3425 coronal lines. The center panel displays the fit for the [Fe VII]λ5722,6085 coronal lines. The bottom panel displays the fit for the broad Hα.

Table 1
Near-IR (Keck NIRSPEC) Emission Line Fluxes

Line	Wavelength (Å)	Flux (10^{-17} erg cm^{-2} s^{-1})
Paα	18756	35.90 ± 1.73
br. Paα	18756	96.72 ± 5.78
Brδ	19451	5.60 ± 1.85
H$_2$	19576	3.86 ± 1.28
[Si VI]	19628	5.69 ± 1.75

Note. Broad lines are identified by "br."

of an AGN, their presence in a BPT star-forming galaxy can often be due to supernova activity, which fades over time (Baldassare et al. 2016). The first observation of J1056+3138 was taken on 2004 May 12, and our Keck observations took place on 2018 March 5. There is a 14 yr baseline between these two observations, so we can explore if there is any fading of the broad lines, which would be indicative of a stellar origin to the broad line rather than an AGN. We compared the extinction corrected optical broad-line flux to the broad Paα flux. The theoretical Hα/Paα ratio, assuming Case B recombination, is 8.5 (Osterbrock & Ferland 2006). The observed value is 6.0 ± 0.1, implying negligible extinction toward the ionized gas, and demonstrating that there is no fading of the recombination line flux over a 14 yr baseline, ruling out the possibility that the broad lines are due to supernova activity. Since we have multiple recombination lines, we also estimated the extinction using the Paα and Brδ lines. Using the observed ratio of these fluxes, we find an $A_V < 1$, assuming a Milky-Way-like extinction curve ($R_V = 3.1$), again implying that there is no fading in recombination line fluxes between the SDSS and near-IR observations.

3.2. X-Ray Results

We detected an X-ray point source coincident with the SDSS optical source with an apparent luminosity, uncorrected for intrinsic absorption, of $L_{X,2-10keV} = (2.3 \pm 0.9) \times 10^{41}$ erg s^{-1}, with six counts combined in both hard and soft bands. Due to the low number of counts, we explored the binomial no-source probability of the detection, P_B, which is proportional to the probability that the measured counts are due to spurious background activity (see Weisskopf et al. 2007; Lansbury et al. 2014 for the mathematical expression for this statistic). Adopting the requirement that real sources (not due to background activity) satisfy a threshold of $P_B < 0.002$ (Satyapal et al. 2017), and noting that the X-ray source yields a no-source probability of $\log(P_B) \sim -6.4$, we conclude that the X-ray source is unlikely to be due to spurious background activity. The typical $L_{2-10keV}$ threshold generally adopted by the community to unambiguously identify an AGN is 10^{42} erg s^{-1} (Zezas et al. 2001; Ranalli et al. 2003; Wang et al. 2013). While the X-ray luminosity for J1056+3138 is somewhat higher than seen in star-forming galaxies, Brorby et al. (2014) find that the X-ray emission produced for a given star-forming rate is approximately an order of magnitude larger than that found in near solar metallicity galaxies (see also Kaaret et al. 2011). Further, Prestwich et al. (2013) also show that ultra-luminous X-ray sources are more common in low-metallicity systems, adding further to the ambiguity of the

Table 2
Optical SDSS Emission Line Fluxes

Line	Wavelength (Å)	Flux $(10^{-17}$ erg cm^{-2} s$^{-1})$
[Ne V]	3345	28.2 ± 11.4
[Ne V]	3426	79.2 ± 9.9
[O III]	4363	65.2 ± 2.8
Hβ	4861	82.7 ± 3.4
br. Hβ	4861	281.6 ± 9.0
[O III]	4959	135.0 ± 4.9
[O III]	5007	407.4 ± 14.7
[Fe VII]	5722	16.0 ± 1.8
[Fe VII]	6085	23.9 ± 2.3
[O I]	6300	10.3 ± 3.0
[N II]	6549	7.0 ± 0.7
Hα	6563	404.5 ± 10.8
br. Hα	6563	578.3 ± 13.1
[N II]	6583	20.5 ± 2.1
[S II]	6717	10.8 ± 1.8
[S II]	6730	7.6 ± 1.4

Note. Broad lines are identified by "br."

origin of the X-ray emission in J1056+3138 and making an AGN identification by this observed X-ray luminosity alone tentative.

The observed luminosity is two orders of magnitude lower than what is expected from the $L_X - L_{12\mu m}$ relation ($\approx 10^{43}$ erg s^{-1}; Secrest et al. 2015). Taking the relation between [Si VI] and L_X from Lamperti et al. (2017), an estimate of $L_X \approx 10^{43}$ is calculated, also two orders of magnitude above the detected luminosity. These discrepancies strongly suggest that the source is heavily obscured along the line of sight. An estimate for N_H was calculated based on the relation determined in R. Pfeifle et al. (2020, in preparation) using 12 μm luminosity data from WISE and X-ray data from the BAT AGN Spectroscopic Survey (BASS), which provides $N_H \approx (7 \pm 2) \times 10^{24}$ cm^{-2}.

We compared this discrepancy between the X-ray and mid-IR luminosities to other similar targets in the MPA/JHU catalog in Figure 6, where we have plotted the L_X/L_{W2} of various mid-IR selected AGNs compared to broad-line AGNs with low metallicity and J1056+3138 compared with their log ([N II]/Hα). Of the low-metallicity galaxies with broad-line AGNs, J1056+3138 has the lowest X-ray luminosity when compared to its W2 luminosity. This apparent deficit in X-ray radiation is in agreement with other X-ray studies done on low-metallicity galaxies, where it is found that X-ray luminosities tend to be one to two orders of magnitude below that expected from multiwavelength diagnostics, due either to obscuration of the X-ray emission or an intrinsic X-ray weakness (Simmonds et al. 2016). This could possibly be due to the lack of an emitting corona, which may be characteristic of a few broad absorption line quasars and ultra-luminous infrared galaxies (Luo et al. 2014; Teng et al. 2015). In addition, for low-mass cases, Dong et al. (2012) found several AGNs in low-mass
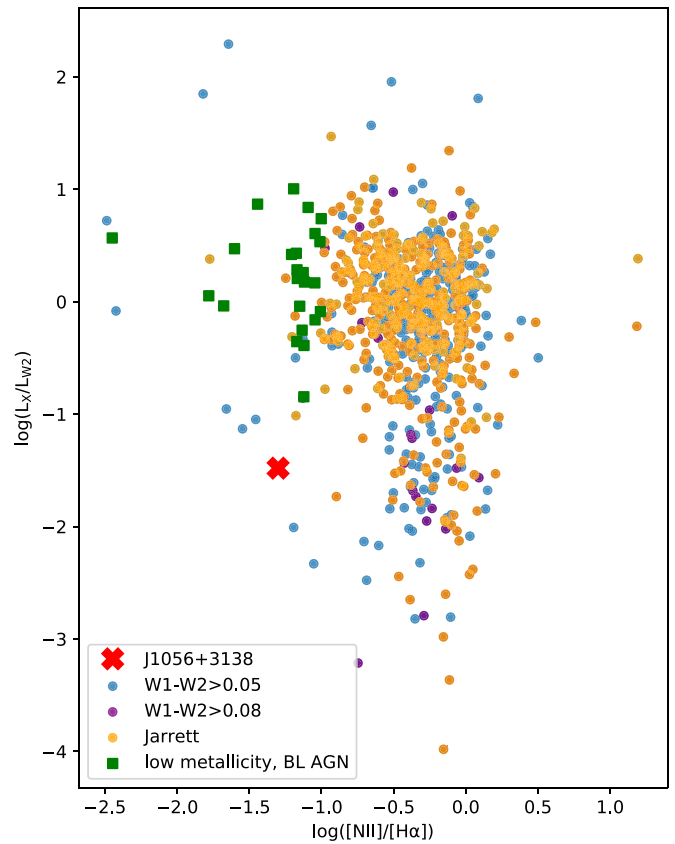
Figure 6. L_X/L_{W2} compared with metallicity diagnostic [N II]/Hα] for galaxies in the MPA/JHU catalog (DR8) that show mid-infrared colors suggestive of AGN activity based on three color cuts: W1–W2 > 0.5 (blue), W1–W2 > 0.8 (purple), and the Jarrett et al. (2011) cut (orange). Galaxies with optical broad lines and [N II]/Hα ratios that fall below the low-metallicity cutoff (log ([N II]/Hα) < − 1.0) are shown as green squares, and J1056+3138 is shown as a red "X." Note that J1056+3138 has the lowest L_X/L_{W2} ratio when compared to similar galaxies.

galaxies that appear to be X-ray weak, possibly due to potential changes in the accretion disk temperature or structure, which would impact the fraction of the disk energy that is reprocessed into a corona. This is supported by the low $L_{X,2-10keV}$ versus $L_{[O III]}$ ratio of several low-mass galaxies in their sample. In J1056+3138, however, the [O III] emission is dominated by star formation, complicating the interpretation of the relationship between these luminosities in this source. It is also possible that there is a different dust-to-gas ratio in this galaxy, potentially affecting the relationship between X-ray absorption and extinction by dust of the broad-line region (Groves et al. 2006). Further, as the WISE and Chandra observations were not simultaneous, with a 9 yr separation between the observations, it is also possible that variability could play a role in this discrepancy, although based on typical flux changes, it may not be able to account for the anomalous ratio found for J1056+3138 (Sheng et al. 2017; Maughan & Reiprich 2019). Due to its low X-ray luminosity, whether due to obscuration, variability, or an inherent X-ray weakness, J1056+3138 would not have been confirmed as an AGN through X-ray follow-up, showing the necessity for multiwavelength studies when dealing with low-mass and low-metallicity galaxies. If even a very powerful AGN can be hidden in the X-rays, many more less powerful and low-luminosity AGNs may be hiding inside low-metallicity dwarf galaxies.

3.3. Black Hole Mass and Luminosity Estimates

Black hole masses were calculated using the widths of the broad Hα (Woo et al. 2015) and Paα (Kim et al. 2018) lines. The broad Paα has a width of 850 ± 25 km s^{-1}, corresponding to a black hole mass of $(2.2 \pm 1.3) \times 10^6\,M_\odot$, or $10^{6.4}M_\odot$, which was obtained with Equation (10) in Kim et al. (2018). In this relation, they used the new virial factor $\log f = 0.05 \pm 0.12$ that was derived in Woo et al. (2015). The broad Hα has a width of 1129 ± 21 km s^{-1}, corresponding to a black hole mass of $(3.4 \pm 1.4) \times 10^6\,M_\odot$, or $10^{6.5}M_\odot$, which was obtained used Equation (5) in Woo et al. (2015).

We estimated the bolometric luminosity of $\approx 10^{44}$ erg s^{-1}, however there is considerable scatter in the $L_{[\text{Si VI}]}$ versus $L_{14-195\,\text{keV}}$ relation reported in Lamperti et al. (2017) with a number of upper limits in their sample. We used a $L_{14-195\,\text{keV}}/L_{\text{bol}}$ factor as reported in Winter et al. (2012). We used the [Si VI] to estimate a bolometric luminosity since the [O III] emission is likely dominated by star formation and cannot be used to obtain a bolometric luminosity as is often done in optically identified AGNs. This luminosity, along with the Eddington luminosities calculated from the mass estimates, implies a high Eddington rate, $L/L_{\text{Edd}} \approx 0.3$. These Eddington ratios are similar to those reported in Greene & Ho (2007) and suggest that this is a highly accreting black hole.

4. Discussion

4.1. Coronal Lines

While coronal lines have often been used as a robust AGN indicator, there is the possibility that these lines arise in star-forming regions. In principle, Wolf–Rayet stars and shock excitation in starburst driven winds can generate broad lines and even high ionization lines (Schaerer & Stasińska 1999; Abel & Satyapal 2008; Allen et al. 2008). Since the hardness of the stellar radiation field increases with decreasing metallicity (Campbell et al. 1986), enhanced emission from lines corresponding to higher ionization potentials is expected for metal deficient galaxies. High ionization lines have indeed been detected in H II regions in blue compact dwarfs (BCDs) and planetary nebulae (Feibelman 1996; Fricke et al. 2001; Thuan & Izotov 2005; Izotov et al. 2012) with a detection rate that appears to be correlated with decreasing metallicity (Izotov et al. 2012). However, the line luminosities are weaker than those found in AGNs, by up to four orders of magnitude (Izotov et al. 2012), and the emission line fluxes are weak compared to the recombination line fluxes. For example, Thuan & Izotov (2005) and Izotov et al. (2012) found [Ne V] emission in 10 H II regions in BCDs, with ratios that range from 0.005 to 0.03 for [Ne V]λ3345/Hβ and from 0.003 to 0.005 for [Ne V]λ3425/Hβ, 3 orders of magnitude below what is found in J1056+3138. Izotov et al. (2001, 2004) also found [Fe VII] emission in two BCD galaxies, with ratios of $\approx$0.001 for [Fe VII] λ5722/Hβ and $\approx$0.0002–0.002 for [Fe VII]λ6085/Hβ, 2–3 orders of magnitude below what is found in J1056+3138. Note that the [Fe VII] and [Ne V] lines in J1056+3138 have luminosities of $\approx 10^{40}$ erg s^{-1}, comparable to those observed in other AGNs, with luminosities ranging from 10^{39} to 10^{42} erg s^{-1} (Malkan 1986; Morris & Ward 1988; Storchi-Bergmann et al. 1995), as is the case for the [Si VI] line as discussed in Section 3. Moreover, while the optical coronal lines have been detected in H II regions and BCDs that may not host AGNs, the ionization potential of Si VI (167 eV) is significantly higher than that of Fe VII or Ne V and is only created in very extreme conditions when not in the presence

of an AGN. Note that this line has been seen in planetary nebulae and Galactic supernovae, but its luminosity is eight orders of magnitude lower than that of J1056+3138 and other AGNs (Ashley & Hyland 1988; Benjamin & Dinerstein 1990; Greenhouse et al. 1990), making these sources undetectable outside of the Milky Way. Thus far, there is no evidence of any coronal line with ionization potential above $\approx$100 eV in a purely star-forming galaxy, making it highly implausible that star formation is responsible for the coronal lines detected in J1056+3138.

4.2. Metallicity Estimates

Current studies of metallicity estimation assume a spectral energy distribution (SED) that is either primarily AGN or stellar in origin. As J1056+3138 hosts an AGN, yet displays star-forming colors and has a strong stellar component, determining a precise SED, and thus a precise estimate of abundances is extremely difficult. However, an initial estimate is calculated using the diagnostics determined by photoionization simulations and tested on low-metallicity dwarf galaxies, including those with AGNs (Izotov et al. 2006, 2007; Izotov & Thuan 2008). This metallicity estimate uses variables t, temperature T_e(O III), C_T, and x as defined by

$$t = \frac{1.432}{\log[\lambda 4959 + \lambda 5007/\lambda 4363] - \log C_T} \quad (1)$$

$$t = 10^{-4} T_e(\text{O III}) \quad (2)$$

$$C_T = (8.44 - 1.09t + 0.5t^2 - 0.08t^3)\frac{1 + 0.0004x}{1 + 0.044x} \quad (3)$$

$$x = 10^{-4} N_e t^{-0.5} \quad (4)$$

where the density, N_e, is 10 (Izotov et al. 2007), as well as emission lines [O III] λ5007, [O III] λ4959, [O II] λ3726, and Hβ. The abundances are then derived using the following:

$$12 + \log \text{O}^+/\text{H}^+ = \log \frac{\lambda 3727}{\text{H}\beta} + 5.961 + \frac{1.676}{t}$$
$$- 0.40 \log t - 0.034t + \log(1 + 1.35x \quad (5)$$

$$12 + \log \text{O}^{2+}/\text{H}^+ = \log \frac{\lambda 4959 + \lambda 5007}{\text{H}\beta} + 6.200$$
$$+ \frac{1.251}{t} - 0.55 \log t - 0.014t. \quad (6)$$

Considering a value of $12 + \log(\text{O/H})$ of 8.69 for solar (Asplund et al. 2006; Groves et al. 2006), these relations provide a metallicity estimate for J1056+3138 of approximately 10% solar. This is in agreement with our initial [N II]/Hα cutoff criteria.

4.3. Implications

The multiwavelength study of J1056+3138 has broad astrophysical implications for our understanding of the origins of SMBHs. J1056+3138 is in one of the lowest metallicity galaxies known to contain an AGN, and it is one of the lowest metallicity, low-mass galaxies to show a high ionization infrared coronal line. While it is a broad-line AGN with strong coronal lines in the optical, its BPT line ratios suggest the dominant emission is stellar in origin. While mid-infrared color selection picks it out as a dominant AGN, with a bright Paα and strong [Si VI] coronal line in its K-band spectrum, it is

barely visible when searching for an X-ray point source, and it would easily be mistaken for X-ray binaries, if it was detected at all. The results presented here strongly support that low-mass accreting black holes exist in galaxies that show no evidence for AGNs using traditional diagnostics, such as X-ray detections and BPT line ratios, calling into question the current occupation of fraction of AGNs in the low-mass and low-metallicity regime and highlighting the importance of multi-wavelength studies to obtain a complete census of AGNs in the low-mass, low-metallicity regime.

Using SDSS and the WISE survey, there are ~1500 low-mass ($M_* < 10^{10.5} M_\odot$), low-metallicity (log (N II/Hα)) galaxies with infrared colors suggestive of AGNs, many of which have stellar masses as low as $10^6 M_\odot$. These are prime candidates for follow-up with the James Webb Space Telescope (JWST) to search for accreting intermediate-mass black holes. None of these galaxies show optical emission line ratios indicative of AGNs, underscoring the limitations of optical studies in the search for accreting black holes in galaxies that may be truly more representative of the local analogs of early galaxies. Currently, there is no direct evidence for black holes with masses anywhere between ≈ 100 and $10,000\ M_\odot$. This technique can be a powerful avenue in which black holes in this "mass desert" can finally be discovered using future high sensitivity JWST observations (Cann et al. 2018). While coronal lines were also seen in the SDSS spectrum of J1056+3138, the predicted fluxes of optical coronal lines are a factor of at least five times less than the infrared coronal lines even in the absence of any extinction (J. Cann et al. 2020, in preparation). The infrared coronal line fluxes are also enhanced when the black hole mass decreases, highlighting the need for infrared spectroscopic observations in the hunt for intermediate-mass black holes (Cann et al. 2018).

5. Conclusions

We present a multiwavelength study of J1056+3138, a low-metallicity, broad-line AGN, including observations from Chandra, Keck/NIRSPEC, WISE, and SDSS. Our main results can be summarized as follows:

1. In its SDSS spectrum, J1056+3138 displays optical emission line ratios suggestive of a purely star-forming galaxy, despite strong optical broad lines and four optical coronal lines, [Ne V]3345,3425 and [Fe VII]5722,6085.

2. Observations with WISE show J1056+3138 to have mid-infrared colors suggestive of a strong AGN, despite only $\approx 0.7\%$ of similarly low-metallicity galaxies residing in the same color–color space.

3. K-band observations with Keck/NIRSPEC revealed a broad Paα line that, when its width and luminosity are compared to that of the broad Hα, implies negligible extinction. These observations also showed a [Si VI] coronal line, making J1056+3138 the lowest metallicity galaxy to show this line.

4. Chandra observations detected an X-ray point source coincident with the SDSS optical source, but at a luminosity of only $\approx 10^{41}$ erg s^{-1}, two orders of magnitude below that expected based on its mid-infrared luminosity. This discrepancy implies the source is either heavily obscured, with an $N_H \approx (7 \pm 2) \times 10^{24}$ cm^{-2}, or inherently X-ray weak.

5. Black hole mass estimates were calculated using the widths of the broad Hα and Paα lines. Estimates ranged

from 2.2 to $3.4 \times 10^6\ M_\odot$, implying this AGN is fairly massive despite its low metallicity.

Our results highlight the need for a multiwavelength approach to truly characterize the source of ionization in this population.

ORCID iDs

Jenna M. Cann ⓘ https://orcid.org/0000-0003-1051-6564
Shobita Satyapal ⓘ https://orcid.org/0000-0003-2277-2354
Remington O. Sexton ⓘ https://orcid.org/0000-0003-3432-2094
Ryan W. Pfeifle ⓘ https://orcid.org/0000-0001-8640-8522
Christina Manzano-King ⓘ https://orcid.org/0000-0002-5253-9433
Barry Rothberg ⓘ https://orcid.org/0000-0003-2283-2185
Mario Gliozzi ⓘ https://orcid.org/0000-0002-8818-9009
Nathan J. Secrest ⓘ https://orcid.org/0000-0002-4902-8077
Laura Blecha ⓘ https://orcid.org/0000-0002-2183-1087

References

Abel, N. P., & Satyapal, S. 2008, ApJ, 678, 686
Allen, M. G., Groves, B. A., Dopita, M. A., Sutherland, R. S., & Kewley, L. J. 2008, ApJS, 178, 20
Appenzeller, I., & Wagner, S. J. 1991, A&A, 250, 57
Ashley, M. C. B., & Hyland, A. R. 1988, ApJ, 331, 532
Asplund, M., Grevesse, N., & Sauval, A. J. 2006, CoAst, 147, 76
Astropy Collaboration, Robitaille, T. P., Tollerud, E. J., et al. 2013, A&A, 558, A33
Baldassare, V. F., Reines, A. E., Gallo, E., et al. 2016, ApJ, 829, 57
Baldwin, J. A., Phillips, M. M., & Terlevich, R. 1981, PASP, 93, 5
Barth, A. J., Greene, J. E., & Ho, L. C. 2008, AJ, 136, 1179
Barth, A. J., Ho, L. C., Rutledge, R. E., & Sargent, W. L. W. 2004, ApJ, 607, 90
Baumgartner, W. H., Tueller, J., Markwardt, C. B., et al. 2013, ApJS, 207, 19
Becker, G. D., Rauch, M., & Sargent, W. L. W. 2009, ApJ, 698, 1010
Benjamin, R. A., & Dinerstein, H. L. 1990, AJ, 100, 1588
Brorby, M., Kaaret, P., & Prestwich, A. 2014, MNRAS, 441, 2346
Campbell, A., Terlevich, R., & Melnick, J. 1986, MNRAS, 223, 811
Cann, J. M., Satyapal, S., Abel, N. P., et al. 2018, ApJ, 861, 142
D'Abrusco, R., Longo, G., & Walton, N. A. 2009, MNRAS, 396, 223
Dawson, K. S., Schlegel, D. J., Ahn, C. P., et al. 2013, AJ, 145, 10
Dong, R., Greene, J. E., & Ho, L. C. 2012, ApJ, 761, 73
Feibelman, W. A. 1996, ApJ, 472, 294
Filippenko, A. V., & Ho, L. C. 2003, ApJL, 588, L13
Foreman-Mackey, D., Hogg, D. W., Lang, D., & Goodman, J. 2013, PASP, 125, 306
Fricke, K. J., Izotov, Y. I., Papaderos, P., et al. 2001, AJ, 121, 169
Gehrels, N. 1986, ApJ, 303, 336
Greene, J. E. 2012, NatCo, 3, 1304
Greene, J. E., & Ho, L. C. 2007, ApJ, 670, 92
Greenhouse, M. A., Grasdalen, G. L., Woodward, C. E., et al. 1990, ApJ, 352, 307
Griffith, R. L., Tsai, C.-W., Stern, D., et al. 2011, ApJL, 736, L22
Groves, B. A., Heckman, T. M., & Kauffmann, G. 2006, MNRAS, 371, 1559
Hamann, F., Korista, K. T., Ferland, G. J., et al. 2002, ApJ, 564, 592
Izotov, Y. I., Chaffee, F. H., & Schaerer, D. 2001, A&A, 378, L45
Izotov, Y. I., Guseva, N. G., Fricke, K. J., et al. 2010, A&A, 517, A90
Izotov, Y. I., Guseva, N. G., Fricke, K. J., & Henkel, C. 2011, A&A, 536, L7
Izotov, Y. I., Papaderos, P., Guseva, N. G., et al. 2004, A&A, 421, 539
Izotov, Y. I., Stasińska, G., Meynet, G., Guseva, N. G., & Thuan, T. X. 2006, A&A, 448, 955
Izotov, Y. I., & Thuan, T. X. 2008, ApJ, 687, 133
Izotov, Y. I., Thuan, T. X., & Guseva, N. G. 2007, ApJ, 671, 1297
Izotov, Y. I., Thuan, T. X., & Privon, G. 2012, MNRAS, 427, 1229
Jarrett, T. H., Cohen, M., Masci, F., et al. 2011, ApJ, 735, 112
Kaaret, P., Schmitt, J., & Gorski, M. 2011, ApJ, 741, 10
Kauffmann, G., Heckman, T. M., Tremonti, C., et al. 2003, MNRAS, 346, 1055
Kewley, L. J., Dopita, M. A., Sutherland, R. S., Heisler, C. A., & Trevena, J. 2001, ApJ, 556, 121
Kim, D., Im, M., Canalizo, G., et al. 2018, ApJS, 238, 37
Koss, M., Trakhtenbrot, B., Ricci, C., et al. 2017, ApJ, 850, 74
Lamperti, I., Koss, M., Trakhtenbrot, B., et al. 2017, MNRAS, 467, 540
Lansbury, G. B., Alexander, D. M., Del Moro, A., et al. 2014, ApJ, 785, 17
Luo, B., Brandt, W. N., Alexander, D. M., et al. 2014, ApJ, 794, 70
Malkan, M. A. 1986, ApJ, 310, 679
Maughan, B. J., & Reiprich, T. H. 2019, OJAp, 2, 9
McLean, I. S., Becklin, E. E., Bendiksen, O., et al. 1998, Proc. SPIE, 3354, 566
Morris, S. L., & Ward, M. J. 1988, MNRAS, 230, 639
Müller-Sánchez, F., Hicks, E. K. S., Malkan, M., et al. 2018, ApJ, 858, 48
Osterbrock, D. E., & Ferland, G. J. 2006, Mercu, 35, 40
Prestwich, A. H., Tsantaki, M., Zezas, A., et al. 2013, ApJ, 769, 92
Rakshit, S., Stalin, C. S., Chand, H., et al. 2017, ApJS, 229, 39
Ranalli, P., Comastri, A., & Setti, G. 2003, A&A, 399, 39
Reines, A. E., Greene, J. E., & Geha, M. 2013, ApJ, 775, 116
Richards, G. T., Myers, A. D., Gray, A. G., et al. 2009, ApJS, 180, 67
Richards, G. T., Myers, A. D., Peters, C. M., et al. 2015, ApJS, 219, 39
Satyapal, S., Secrest, N. J., Ricci, C., et al. 2017, ApJ, 848, 126
Schaerer, D., & Stasińska, G. 1999, A&A, 345, L17
Schramm, M., Silverman, J. D., Greene, J. E., et al. 2013, ApJ, 773, 150
Secrest, N. J., Satyapal, S., Gliozzi, M., et al. 2015, ApJ, 798, 38
Sexton, R. O., Canalizo, G., Hiner, K. D., et al. 2019, ApJ, 878, 101
Sheng, Z., Wang, T., Jiang, N., et al. 2017, ApJL, 846, L7
Simmonds, C., Bauer, F. E., Thuan, T. X., et al. 2016, A&A, 596, A64
Souchay, J., Andrei, A. H., Barache, C., et al. 2012, A&A, 537, A99
Souchay, J., Andrei, A. H., Barache, C., et al. 2015, A&A, 583, A75
Stern, J., & Laor, A. 2013, MNRAS, 431, 836
Storchi-Bergmann, T., Kinney, A. L., & Challis, P. 1995, ApJS, 98, 103
Storchi-Bergmann, T., Schmitt, H. R., Calzetti, D., & Kinney, A. L. 1998, AJ, 115, 909
Taylor, M. B. 2005, in ASP Conf. Ser. 347, Astronomical Data Analysis Software and Systems XIV, ed. P. Shopbell, M. Britton, & R. Ebert (San Francisco, CA: ASP), 29
Teng, S. H., Rigby, J. R., Stern, D., et al. 2015, ApJ, 814, 56
Thuan, T. X., & Izotov, Y. I. 2005, ApJS, 161, 240
Toba, Y., Oyabu, S., Matsuhara, H., et al. 2014, ApJ, 788, 45
van Wassenhove, S., Volonteri, M., Walker, M. G., & Gair, J. R. 2010, MNRAS, 408, 1139
Vergani, D., Garilli, B., Polletta, M., et al. 2018, A&A, 620, A193
Volonteri, M., & Begelman, M. C. 2010, MNRAS, 409, 1022
Volonteri, M., & Natarajan, P. 2009, MNRAS, 400, 1911
Wang, S. X., Brandt, W. N., Luo, B., et al. 2013, ApJ, 778, 179
Weisskopf, M. C., Wu, K., Trimble, V., et al. 2007, ApJ, 657, 1026
Winter, L. M., Veilleux, S., McKernan, B., et al. 2012, ApJ, 745, 107
Woo, J.-H., Yoon, Y., Park, S., Park, D., & Kim, S. C. 2015, ApJ, 801, 38
Yan, L., Wang, T., Jiang, N., et al. 2019, ApJ, 874, 44
Zezas, A., Alonso-Herrero, A., & Ward, M. J. 2001, Ap&SS, 276, 601